AIMS Materials Science, 11(5): 991–1012.
DOI: 10.3934/matersci.2024047
Received: 11 July 2024
Revised: 26 August 2024
Accepted: 03 September 2024
Published: 25 October 2024

https://www.aimspress.com/journal/Materials

Research article

Citrate coated iron oxide nanoparticles: Synthesis, characterization, and performance in protein adsorption

Denise Arrozarena Portilla[1], Arturo A. Velázquez López[2], Rosalva Mora Escobedo[2,*] and Hernani Yee Madeira[1,*]

[1] Laboratorio de Espectroscopía Mossbauer y Técnicas Complementarias, Departamento de Física, Escuela Superior de Físico Matemáticas, Instituto Politécnico Nacional, Ciudad de México 07738, México

[2] Laboratorio de Bioquímica de la Nutrición, Departamento de Ingeniería Bioquímica, Escuela nacional de Ciencias Biológicas, Instituto Politécnico Nacional, Ciudad de México 07738, México

* **Correspondence:** Email: hyeem@ipn.mx; rmorae@ipn.mx; Tel.: +52-55-5432-8639; +52-55-3432-1489.

Abstract: Magnetic nanoparticles (MNPs) are extensively utilized in biomedicine as part of controlled drug release systems, hyperthermia, and magnetic resonance imaging. Surface modification of MNPs not only enhances their stability and biocompatibility but also increases affinity with certain molecules, allowing them to be used in protein separation and adsorption processes. This article reports the synthesis and characterization of iron oxide MNPs functionalized with citric acid (IONPs@CA) to evaluate their performance in protein adsorption. The nanoparticles were characterized using various techniques such as transmission electron microscopy (TEM), X-ray diffraction (XRD), dynamic light scattering (DLS), thermogravimetric analysis (TGA), and Fourier-transform infrared spectroscopy (FT-IR). The percentage of lysozyme (Lyz) adsorbed by IONPs@CA was 84.9%, while the IONPs sample only adsorbed 5.9%. In silico evaluation results showed some repulsion bonds obtained in Lyz-IONPs and hydrogen bonds, carbon-hydrogen bonds, and van der Waals interactions in Lyz-IONPs@CA. These results may be novel since no previous research was found specifying this type of interaction between lysozyme and IONPs and/or IONPs@CA. The maximum adsorption efficiency obtained for the coated nanoparticles was 88.3%.

Keywords: iron oxide nanoparticles; citric acid functionalization; protein purification; in silico study

Abbreviations: ASN: Asparagine; ATR-FT-IR: Attenuated total reflection Fourier-transform infrared spectroscopy; DLS: Dynamic light scattering; GLU: Glutamine; ILE: Isoleucine; IONPs: Iron oxide nanoparticles; IONPs@CA: Citric acid coated iron oxide nanoparticles; LYS: Lysine; Lyz: Lysozyme; MNP: Magnetic nanoparticles; PDB: Protein database; RCSB: Research Collaboratory for Structural Bioinformatics; SER: Serine; TEM: Transmission electron microscopy; TGA: Thermogravimetric analysis; TRP: Tryptophan; UCSF: University of California, San Francisco; VAL: Valine; XRD: X-ray diffraction

1. Introduction

Protein purification processes are widely employed in various biotechnology areas, aiming primarily to separate proteins from the complex mixtures in which they are naturally present. Purification is crucial when structurally and functionally characterizing proteins of interest. Ultrafiltration [1], electrophoretic separation [2], precipitation [3], and chromatography [4] are among the most used techniques for protein isolation. Chromatography, particularly affinity chromatography, is favored by researchers due to its high selectivity [5]. In affinity chromatography, separation occurs due to the various interactions that a protein can have with specific ligands. Antigen–antibody binding and recognition between an enzyme and its substrate are among these interactions [6]. Peptides [7,8], synthetic oligonucleotides [9,10], metal ions [11–14], and antibodies [15] are among the most used affinity ligands for protein isolation. However, these processes have limitations such as time consumption and the need for expensive instrumentation [16,17].

Magnetic separation emerges as an alternative to conventional procedures due to its easy implementation and few steps, which can be carried out in one or two vials at most. Other advantages include the ability to work directly with crude samples without prior treatment [18] and maintaining protein integrity after purification [19]. Magnetic carriers with immobilized ligands on their surface are used for separation. These carriers are added to the desired mixture to achieve protein binding and, subsequently, the entire complex can be isolated using an external magnetic field [20].

Magnetic nanoparticles (MNPs), mainly magnetite (Fe_3O_4) and maghemite (γ-Fe_2O_3), are the most used magnetic carriers in recent years. Properties such as rapid response to a magnetic field, large surface area, and mechanical stability make MNPs attractive for magnetic separation [21]. Their nanoscale size gives them superparamagnetic properties, meaning they exhibit no residual magnetization once the external magnetic field is removed [22]. However, their use in biotechnology depends heavily on their colloidal stability. Therefore, most authors reporting MNP applications in biotechnology work with MNPs coated with stabilizing agents, which not only improve colloidal stability but also enhance biocompatibility and reduce nanoparticle toxicity [23–26].

In recent years, several researchers have utilized magnetic materials for protein purification and/or immobilization (e.g., antibodies and enzymes). Zeng et al. (2020) developed Ni(II)-chelated Fe_3O_4 nanoparticles to immobilize proteins tagged with polyhistidine [27]. They found that the nanoparticles could be reused up to six times without affecting the activity of the immobilized protein. Lodhi et al. (2022) reported an innovative affinity purification method for exopolygalacturonase (Exo-PG) using Fe_2O_3 magnetic nanoparticles superficially modified with galacturonic acid [28]. Tavakoli et al. (2019) synthesized mesoporous silica-coated magnetic nanoparticles for recombinant protein separation, achieving a maximum adsorption capacity of 235.21 μg of protein per milligram of nanoparticles [29].

Most of these studies are based on affinity principles, utilizing polymeric molecules or, in some cases, double functionalization of nanoparticles to enhance protein adsorption. This work proposes a simpler method for Lyz adsorption onto iron oxide nanoparticles through citrate functionalization. This coating can enhance the interaction between nanoparticles and proteins, facilitating their immobilization.

2. Materials and methods

2.1. Materials

Ferric chloride hexahydrate ($FeCl_3 \cdot 6H_2O \geq 98\%$), anhydrous citric acid [$HOC(COOH)(CH_2COOH)_2$, 99%], ferrous chloride tetrahydrate ($FeCl_2 \cdot 4H_2O$, 99%), dibasic sodium phosphate (Na_2HPO_4, ACS ≥ 99%), monobasic potassium phosphate (KH_2PO_4, suitable for cell culture, ≥99%), and chicken egg lysozyme (Lyz, ≥90%) were sourced from Sigma-Aldrich. Hydrochloric acid (HCl, PA) and sodium hydroxide (NaOH, a.c.s) were obtained from Fermont.

2.2. Synthesis of iron oxide nanoparticles and subsequent citric acid coating

Iron oxide nanoparticles (IONPs) were synthesized following the procedure described by Medina-Espinosa (2021) with some modifications. A solution of NaOH (0.9 mol/L) was prepared, to which a mixture of $FeCl_3 \cdot 6H_2O$ (1.28 mol/L), $FeCl_2 \cdot 4H_2O$ (0.64 mol/L), and HCl (0.4 mol/L) [30] was added dropwise using a peristaltic pump at 48 rpm. The reaction mixture was kept in an ultrasonic bath under a nitrogen atmosphere and mechanical agitation (450 rpm) for 30 min at room temperature. After completion of the reaction, the pH of the mixture was approximately 12. The product was collected using a neodymium magnet, washed three times with distilled water, and vacuum dried.

Subsequently, 250 mg of nanoparticles were re-dispersed in 200 mL of deionized water, and the pH was adjusted to 10. Then, 1 mL of an aqueous solution of citric acid (0.25 g/mL) was added, and the mixture was mechanically stirred for 6 h [31]. After this time, the citric acid-coated nanoparticles (IONPs@CA) were collected magnetically, washed with deionized water, and vacuum-dried. Characterization techniques (specifically, FT-IR, DLS, and TGA) showed indications of the presence of coating on the surface of the nanoparticles. Details of these results are discussed below.

2.3. Characterization of nanoparticles

Both IONPs and IONPs@CA were analyzed using different characterization techniques. XRD was performed using a Bruker diffractometer (Bruker, D8 Advance, Germany). The diffraction patterns were recorded using Cu-Kα ($\lambda = 1.54183$ Å) as incident radiation, in a range of 10–90°, with an increment of 0.02°; the counting speed was set to 10 s per point. ATR-FT-IR was carried out on a PerkinElmer spectrometer (PerkinElmer, FRONTIER, USA); spectra were acquired in the range of 400–4000 cm^{-1}. The morphology and size of the nanoparticles were determined using TEM. Images were obtained on a JEOL microscope (JEOL, JEM-2100, Japan); for this, a sample of nanoparticles was sonicated in 2-propanol, deposited on a carbon-copper grid, and allowed to dry overnight. TGA was conducted using a Netzsch thermogravimetric analyzer (Netzsch, STA 409 PC Luxx, Germany). During this analysis, samples were heated to 900 °C at a rate of 20 °C/min under an inert argon atmosphere. The hydrodynamic diameter and zeta potential of the nanoparticles were determined by

DLS using a Zetasizer Nano sampler (Malvern Instruments, Zetasizer Nano ZS, UK) equipped with a He-Ne laser (λ = 633 nm). Hydrodynamic diameter measurement of the nanoparticles was performed at 25 °C in a range of 0.3–10 μm using polystyrene cuvettes. Samples were at a concentration of 0.1% (w/v), and water was used as the dispersing medium. Zeta potential determination was carried out using 0.1 M phosphate buffer (pH 7.4). Protein quantification was performed according to the Bradford method [32] using a Thermo Scientific microplate reader (Thermo Scientific, Multiskan GO, USA).

2.4. Protein adsorption

The adsorption assay was conducted following the method reported by Rahman et al. (2012) with some modifications. A Lyz solution (1.5×10^{-5} mol/L) in 0.1 mol/L phosphate buffer (pH 7.4) was prepared. Both nanoparticle samples (IONPs and IONPs@CA) were used for the adsorption experiment. Approximately 5 mg of nanoparticles were added to 5 mL of the working solution, and the mixture was mechanically stirred for 4 h [33]. After this time, the protein content in the supernatant was determined using the Bradford assay [32]. In a 96-well microplate, 100 μL of the supernatant and 100 μL of the Bradford reagent were added, and after 10 min of incubation, absorbance at 595 nm was read. Protein quantification was carried out using a bovine serum albumin calibration curve. The percentage of Lyz adsorbed by the nanoparticles was calculated as expressed in Eq 1:

$$adsorption\% = \frac{C_0 - C_f}{C_0} \times 100 \quad (1)$$

where C_0 and C_f are the initial and final concentrations, respectively, of Lyz expressed in μg/mL [34].

Under these conditions, the IONPs@CA sample adsorbed the greater amount of protein; therefore, it was chosen to evaluate its maximum adsorption capacity. For this purpose, a total of seven Lyz solutions were prepared, ranging in concentrations from 5.8 to 23.6 μg/mL. Aliquots of 1 mL from each solution were taken and placed in seven different 1.5 mL vials, each containing, approximately 1.5 mg of IONPs@CA. The mixtures were stirred for 4 h, and after this time, the remaining protein concentration in the supernatant after adsorption was determined using the Bradford method [32].

2.5. In silico evaluation by molecular docking

The crystalline structure of lysosome (PDB code: 1AT5) was obtained from the RCSB Protein Data Bank (PDB), while magnetite and citrate were obtained using simplified molecular-input line-entry system (SMILE) sequences and modeled in AutodockTools 1.5.7. AutoDock 4.2 was employed to investigate the interactions between magnetite, citrate, and lysozyme. Initially, the structures of magnetite and citrate were drawn using Avogadro, and their geometries were optimized using AutoDock 4.2. Prior to docking analysis, hydrogen atoms and water molecules were removed from the protein, and energy minimization was performed using UCSF Chimera 1.15. For the docking calculations in AutoDock 4.2, the Lamarckian genetic algorithm was utilized, with grid parameters set to 130 × 130 × 130 and a spacing of 1 Å. To determine the binding sites on lysozyme, the ligands were allowed to move within the grid region through 50 runs to explore potential binding conformations. Additionally, the docked complex structures of the ligands and the surrounding amino acid residues were analyzed using BIOVIA Discovery Studio Visualizer.

2.6. Statistical analysis

Experiments were conducted in triplicate and expressed as mean values and their standard deviations. A significance level of $p \leq 0.05$ was employed for all samples. The data were analyzed using RStudio version 1.4.2.1.

3. Results and discussion

3.1. Synthesis of iron oxide nanoparticles and subsequent citric acid coating

Nanoparticles were synthesized using the coprecipitation method, resulting in a black solid (magnetite) [34]. However, the presence of atmospheric oxygen can cause the oxidation of Fe_3O_4, leading to the formation of γ-Fe_2O_3, which is a brown solid [35]. To prevent this phenomenon, the reaction was carried out in an inert nitrogen (N_2) atmosphere. The reaction involved in the formation of magnetite, as the main product, is represented in Eq 2. During synthesis, in addition to classical mechanical stirring, ultrasonic agitation was employed, which may contribute to obtaining nanoparticles with homogeneous size distribution compared to those obtained through conventional coprecipitation [36]. The coating of IONPs with citric acid was carried out at pH 10 to ensure the formation of carboxylate groups on the surface of the nanoparticles, which enhance their colloidal stability [37] and facilitate protein adsorption [38].

$$2Fe^{3+}_{(aq)} + Fe^{2+}_{(aq)} + 8OH^{-}_{(aq)} = Fe_3O_{4_{(s)}} + 4H_2O \quad (2)$$

3.2. Characterization of nanoparticles

3.2.1. X-ray diffraction (XRD)

Figure 1 shows the XRD pattern of nanoparticles with and without coating. Both patterns can be associated with the inverse spinel cubic structure of magnetite and maghemite [39]. The main peaks are observed at the following positions: 30.2, 35.6, 43.3, 53.6, 57.3, 62.9°. These peaks can be indexed to the planes (hkl) (220), (311), (400), (422), (511), and (440), respectively, according to the standard pattern of magnetite (JCPDS 19629). No differences are observed when comparing the diffraction patterns of both samples, suggesting that the coating process does not affect the crystalline structure of the nanoparticles [40]. The crystallite size and lattice parameter for each sample were estimated using High Score Plus (3.0.2) software, which utilizes Rietveld refinement for the estimations (see Figures S1 and S2 and Tables S1 and S2). The estimated crystallite size for IONPs was 7.9 and 7.6 nm for IONPs@CA. These values are lower than those generally obtained when NH_4OH is used as a base during the coprecipitation reaction [41,42]. The difference in sizes can be explained by considering that NaOH is a strong base, which promotes nucleation but affects the growth of the nuclei, resulting in a large number of small-sized particles [43]. Furthermore, the lattice parameter value obtained for IONPs was 8.367 ± 0.005 Å, which falls between the values for maghemite and magnetite (8.3515 and 8.3960 Å) [44] and 8.357 ± 0.002 Å for IONPs@CA. The reduction in the lattice parameter of the nanoparticles after functionalization may occur due to the interaction between the coating atoms and the nanoparticle's atoms, causing the contraction in the crystal lattice [45]. Some authors also report

this variation in the lattice parameter of nanoparticles after functionalization [41,42]. Although the black color of the synthesized IONPs suggests the presence of Fe_3O_4, the nanometric nature of the material facilitates its oxidation to γ-Fe_2O_3 upon exposure to atmospheric oxygen. Distinguishing between magnetite and maghemite using XRD can be challenging because both phases possess very similar crystal structures and nearly identical lattice parameters, leading to almost indistinguishable diffraction patterns; therefore, we assume that the synthesized iron oxide nanoparticles are a mixture of both phases.

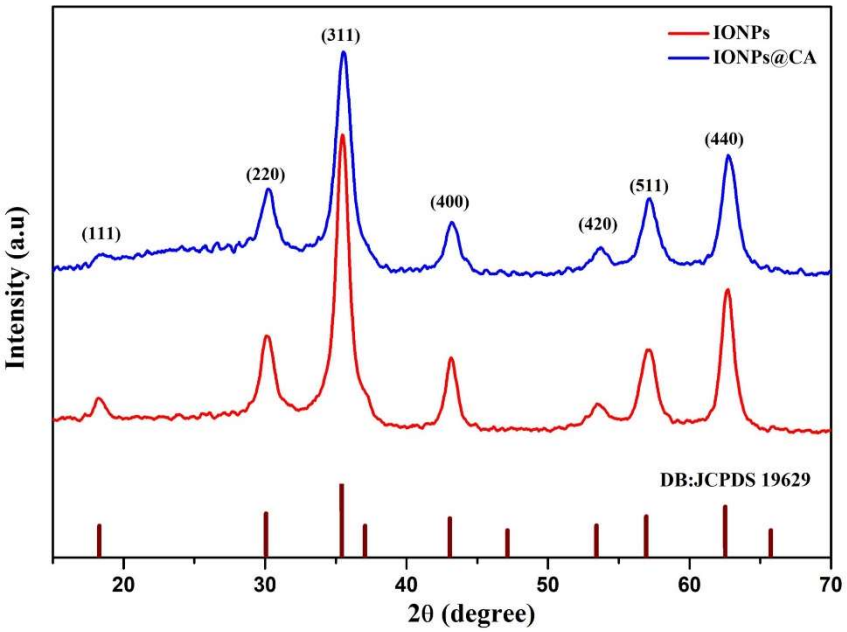

Figure 1. XRD pattern of IONPs and IONPs@CA.

3.2.2. Fourier-transform infrared spectroscopy

The IR spectra of IONPs and IONPs@CA samples are presented in Figure 2. For IONPs, an intense signal is observed near 545 cm^{-1}, assignable to the stretching vibration of the Fe–O bond [46], thus confirming the formation of iron oxide. Near 3404 cm^{-1}, a broad and weak band corresponding to the O–H group of water present on the material's surface is observed. In the spectrum of IONPs@CA, the band near 558 cm^{-1} indicates the presence of an iron oxide core as it corresponds to the Fe–O bond. The slight shift of this signal compared to IONPs can be explained by the binding of carboxylate groups to the nanoparticles, causing variations in the vibration frequencies of the bond between iron and oxygen atoms. Lastly, the bands observed near 1577 and 1390 cm^{-1} can be attributed to the asymmetric and symmetric stretching vibrations of the carboxylate group, respectively. The presence of these signals confirms the formation of citrate coating on the surface of the nanoparticles [37,38,46,47].

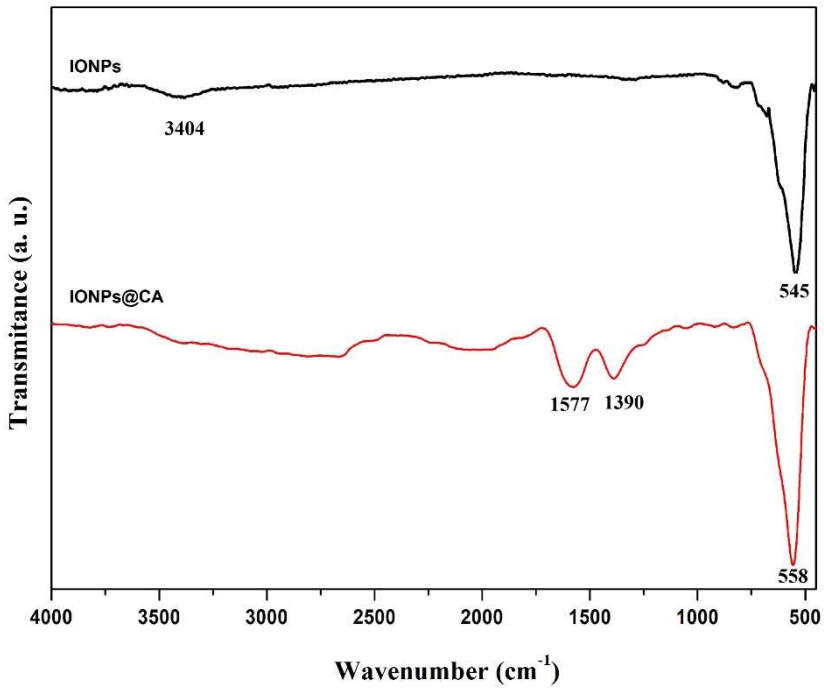

Figure 2. FT-IR of IONPs and IONPs@CA.

3.2.3. Transmission electron microscopy

In Figure 3, micrographs of both samples along with the corresponding histograms are presented. The images reveal the tendency of both samples to form agglomerates. Despite this, in both images, some individual particles within the agglomerate can be distinguished, which exhibit nearly spherical morphology. Particles' average size is approximately 8 nm for both samples, making them suitable for biomedical applications [48,49]. This similarity in size between IONPs and IONPs@CA aligns with findings reported by Li et al. (2013) and Atrei et al. (2021). These authors demonstrated that the post-synthesis coating process has no significant effects on the size of the nanoparticles [50,51]. Furthermore, this value is very close to the crystallite size obtained via XRD (see Table 1) after Rietveld refinement; so, this observation could provide evidence of the formation of a monocrystalline material [41].

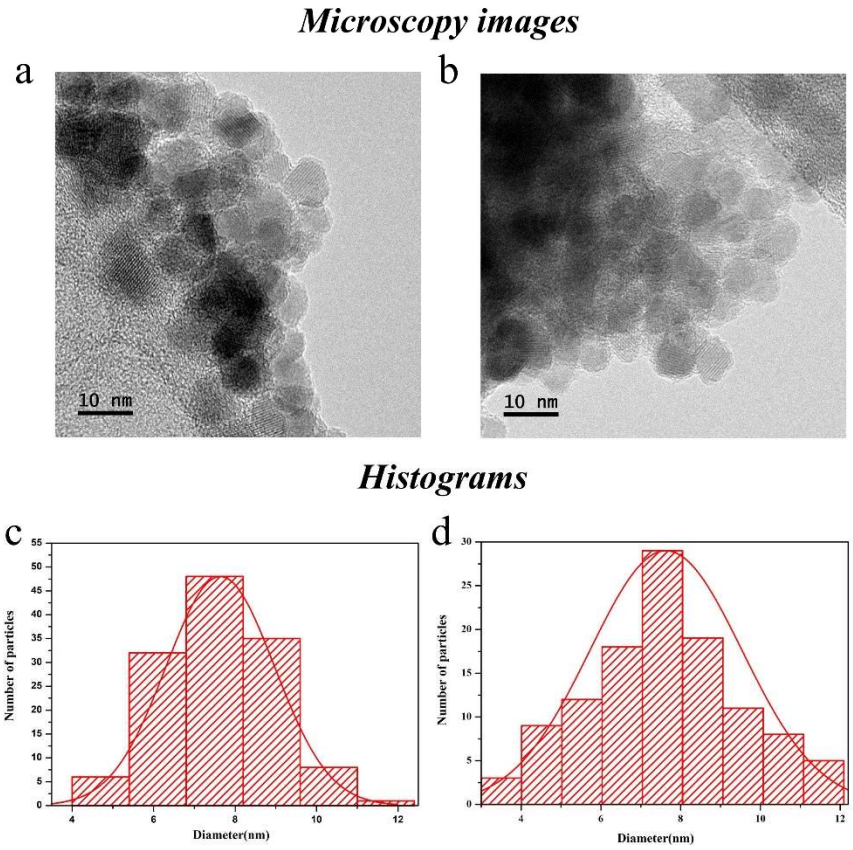

Figure 3. Microscopy images: (a) IONPs, (b) IONPs@CA. Histograms: (c) IONPs, (d) IONPs@CA.

Table 1. Particle size according to XRD and TEM.

Sample	Crystallite size (nm)	TEM size (nm)
IONPs	7.9 ± 0.2*	7.58 ± 0.06^{+}
IONPs@CA	7.6 ± 0.5*	7.56 ± 0.11^{+}

*Estimated standard deviation (from Rietveld refinement); $^{+}$standard error.

Determining the size of nanoparticles is crucial for our objectives, as this parameter significantly influences the magnetic behavior of the sample [52]. In our case, it is desirable for the nanoparticles to behave as superparamagnetic material. However, since we do not have magnetic characterization, we analyzed published works on the subject to reach a conclusion. As can be seen, both IONPs and IONPs@CA have particle sizes below 20 nm, which is considered the critical size for nanoparticles to exhibit superparamagnetic behavior [53]. There is sufficient evidence that nanoparticles with diameters below this critical value exhibit superparamagnetic properties [54–57]. On the other hand, organic coatings can also affect the magnetic behavior of nanoparticles [58]. Some authors have assessed this effect. For instance, Li et al. (2013) obtained magnetite samples coated with citric acid at different coating percentages (5.2% and 3.5%) [50]. Magnetic characterization at room temperature showed no hysteresis, which is a unique characteristic of superparamagnetic materials [59], for the

sample with 5.2% coating. Similar results have been reported by Omelyanchik et al. (2021) and Blanco-Andujar (2015) [60,61]. It is important to note that this bibliographic analysis focused on magnetic measurements conducted at room temperature, as our adsorption experiments were performed at the same temperature. Therefore, it can be assumed that the samples obtained in this work possess superparamagnetic properties, which is advantageous for our purposes; due to the absence of remanent magnetization, once the external magnetic field is removed, the nanoparticles do not agglomerate, facilitating their use in subsequent purification cycles and making them easier to handle.

Furthermore, the adsorption is also affected by the size of the nanoparticles. Various authors who have investigated this topic conclude that the number of adsorbed molecules per unit of mass of nanoparticles increases as their size decreases [62,63]. As the diameter of the nanoparticles decreases, their specific surface area increases, leading to a higher number of active sites available for the adsorption of molecules with which they come into contact [62].

Thus, the particle size in our samples could ensure the formation of more carboxylate groups during coating, thanks to their increased specific surface area, which in turn would increase the adsorption capacity of the nanoparticles.

3.2.4. Thermogravimetric analysis

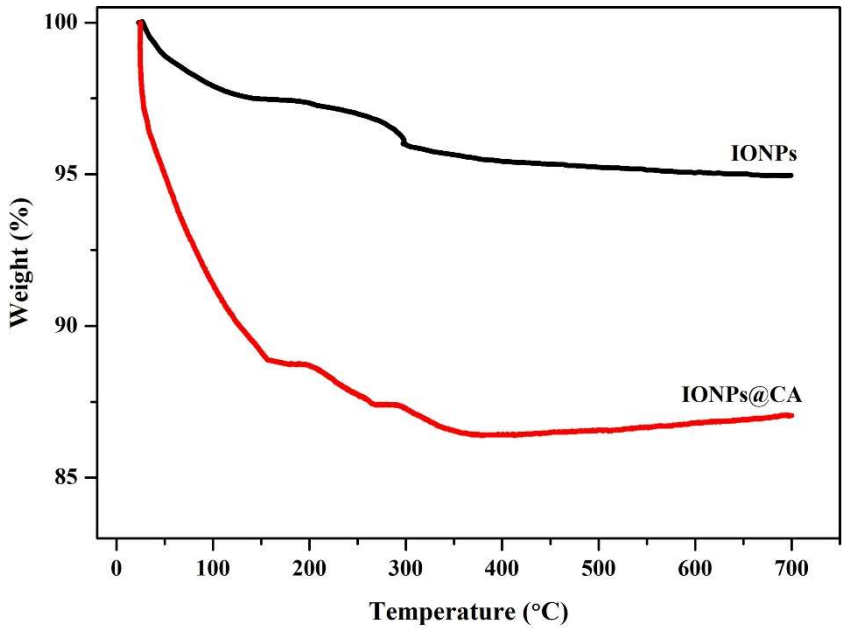

Figure 4. TGA curves of IONPs and IONPs@CA.

The TGA technique allows the evaluation of both the thermal stability and composition of materials, and it can be used to determine the amount of coating present on the surface of nanoparticles [64]. The curve of percentage mass loss as a function of temperature is depicted in Figure 4. For IONPs, the mass loss throughout the analysis interval was only 4.4%. This loss may be attributed to the evaporation of chemically and physically adsorbed water molecules [65]. IONPs@CA, on the other hand, exhibited a total mass loss of 13.6%. Up to 160 °C, the mass loss in this sample can be attributed to the evaporation of physically adsorbed water on the surface of the nanoparticles; the mass loss observed from 160 °C to approximately 350 °C may correspond to the decomposition of the citrate

coating the nanoparticle surface [47]. The difference between the mass loss percentages for each sample (13.6% for IONPs@CA and 4.4% for IONPs) can be used to estimate the percentage of citrate present in the coated nanoparticles, with this value being 9.2%. Previous studies report similar results [66,67].

3.2.5. Dynamic light scattering and zeta potential

The DLS technique allows the determination of the hydrodynamic diameter of both individual particles and agglomerates of particles moving independently in a suspension [68]. The particle sizes obtained for the IONPs and IONPs@CA samples are shown in Table 2. The large difference between these results and the individual particle size (8 nm) suggests the formation of particle agglomerates in both samples, which can be confirmed by TEM images. Additionally, the table presents the values of the zeta potential for both samples. This parameter is widely used as an indicator of the colloidal stability of a suspension. A suspension with an absolute zeta potential value greater than 30 mV is considered highly stable [69], while suspensions with a zeta potential below this value tend to form agglomerates and flocculate due to Van der Waals forces causing particle attraction [70]. The zeta potential value for the IONPs sample was −28.90 ± 0.52 mV, while for IONPs@CA it was −31.65 ± 0.57 mV. This variation in the zeta potential value, after coating with citric acid, is consistent with previous research findings [71,72] and can be explained by the increase in negative charges on the surface of the nanoparticles caused by the presence of carboxylate groups. This increase in charges enhances the electrostatic repulsion between nanoparticles, reducing the tendency for aggregation and increasing the stability of the suspension [71]. In addition, the sign of the zeta potential (positive or negative) is often associated with the surface charge of the nanoparticles [73]. In our case, the nanoparticles have a negative zeta potential, which promotes interaction with lysozyme, as it is positively charged at pH 7.4 (the pH selected for the adsorption assays).

Table 2. Particle size according to DLS and Z potential (values are reported as mean ± standard deviation).

Sample	D_h (nm)	Z potential (mV)
IONPs	311 ± 21	−28.90 ± 1.65
IONPs@CA	482 ± 21	−31.65 ± 1.82
Lysozyme	-	+6.47 ± 0.83

3.3. Protein adsorption

The aim of this assay was to verify whether the presence of carboxylate groups (derived from the coating with citric acid) had any effect on the amount of protein adsorbed by the nanoparticles. Lyz was chosen for these tests as it is a protein with an isoelectric point in the range of 9.5–11.0 [74]; hence, at pH 7.4, it carries a positive charge, as shown in Table 2. After 4 h of interaction between the dissolved Lyz and the nanoparticles (IONPs and IONPs@CA), the percentage of adsorbed Lyz was determined for both samples, and the results are shown in Figure 5.

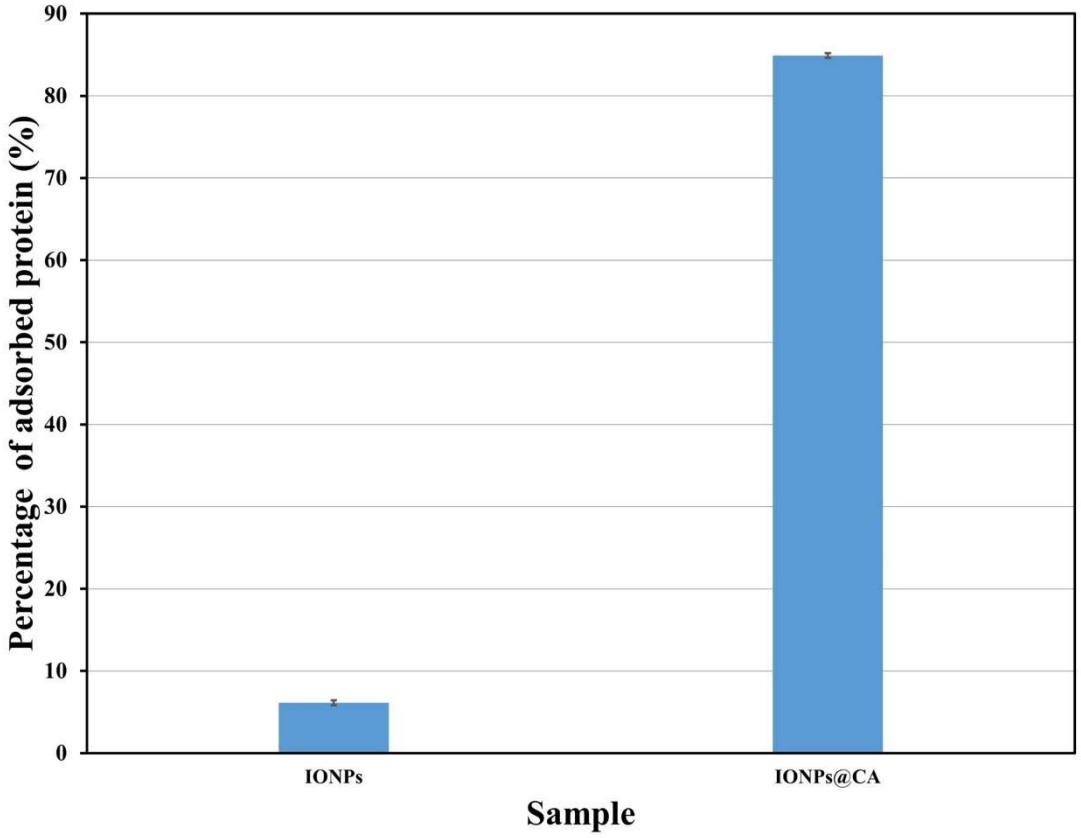

Figure 5. Percentage of protein adsorbed by nanoparticles.

The results demonstrate that both IONPs and IONPs@CA undergo Lyz adsorption, albeit to different extents. The adsorption yield for uncoated nanoparticles was 6.1 ± 0.3%, while for coated nanoparticles, the yield was 84.9 ± 0.3%. This difference can be attributed to the introduction of new functional groups on the nanoparticle surface, which increases the number of potential interaction sites between lysozyme and the nanoparticles.

3.3.1. In silico evaluation by molecular docking

Molecular docking was conducted to analyze the mechanistic interactions of IONPs and IONPs@CA for binding with Lyz. Currently, molecular docking has garnered interest as a computational tool capable of predicting interactions and binding energies between ligands and target macromolecules, facilitating optimal binding selection [75]. The cubic structure of IONPs, confirmed via XDR analysis, is depicted in Figure 6. During in silico evaluation, 50 IONPs-Lyz and 50 citrate-Lyz dockings were obtained. Figure 6 (and Table S3) illustrates the most stable IONPs-Lyz docking, yielding a binding energy of −3.98 kcal/mol and an inhibition constant of 1.21 mM. The primary amino acids of lysozyme involved in interactions with IONPs are asparagine (ASN), glutamine (GLN), and tryptophan (TRP). ASN binds to IONPs through conventional hydrogen bonds and metal–acceptor interactions. Similarly, GLN engages in metal–acceptor interactions, while TRP can act as an electron density donor due to the indole ring present in its structure. However, molecular docking results indicate that interactions such as bump and metal–donor may also occur between lysozyme and IONPs, potentially affecting the stability of the docking configuration [76,77].

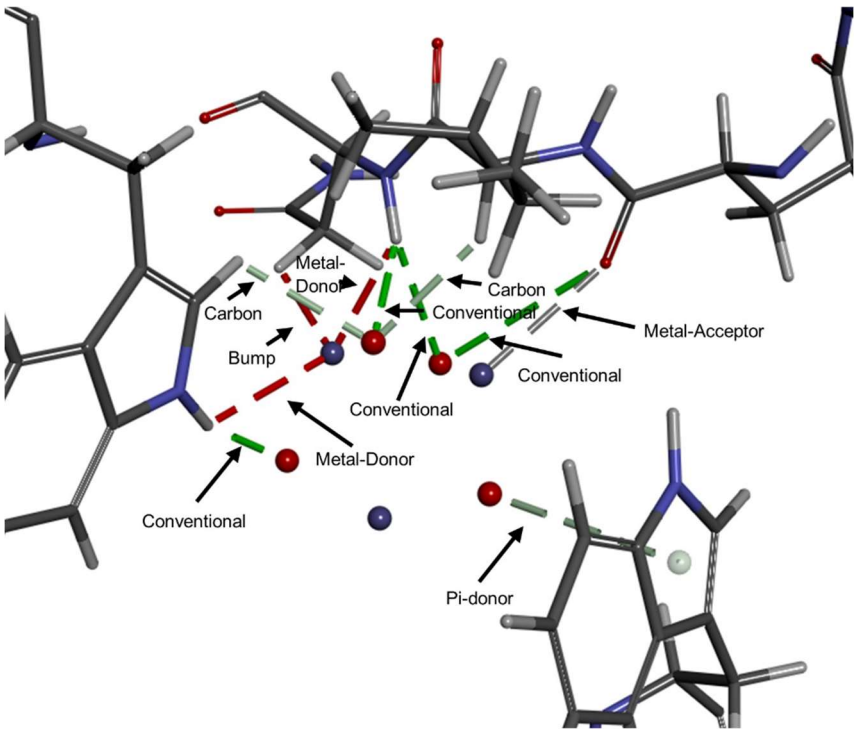

Figure 6. IONPs and Lyz coupling.

Distinct outcomes were obtained from citrate-Lyz dockings, exhibiting varying binding energies and inhibition constants. Figure 7 displays the formation of predominantly stable bonds, compared to those formed with IONPs. We can highlight the potential hydrogen bonds that may form between isoleucine (ILE), valine (VAL), and lysine LYS with citrate; carbon-hydrogen bonds promoted by interactions with ASN at position 103 of lysozyme; and van der Waals interactions (involving TRP, serine (SER), and LYS), which collectively contribute to the increased stability of the binding. These results are comparable to those obtained by Vaidyanathan et al. (2023) in their study on the interactions between human serum albumin (HSA) and phenolic acid derivatives. The authors report interactions involving TRP, SER, and LYS with the $–COO^-$ group [78]. Docking 19 (Figure 7a) yielded binding energy of –4.81 kcal/mol, docking 11 of –4.56 kcal/mol (Figure 7b), and docking 44 of –4.51 kcal/mol (Figure 7c). Compared to the binding energy of IONPs docking, these values are significantly lower, indicating that Lyz exhibits greater affinity for IONPs@CA than IONPs [79]. Moreover, no unfavorable interactions were observed between citrate and the protein; this demonstrates the superior performance of IONPs@CA during lysozyme adsorption in comparison to IONPs.

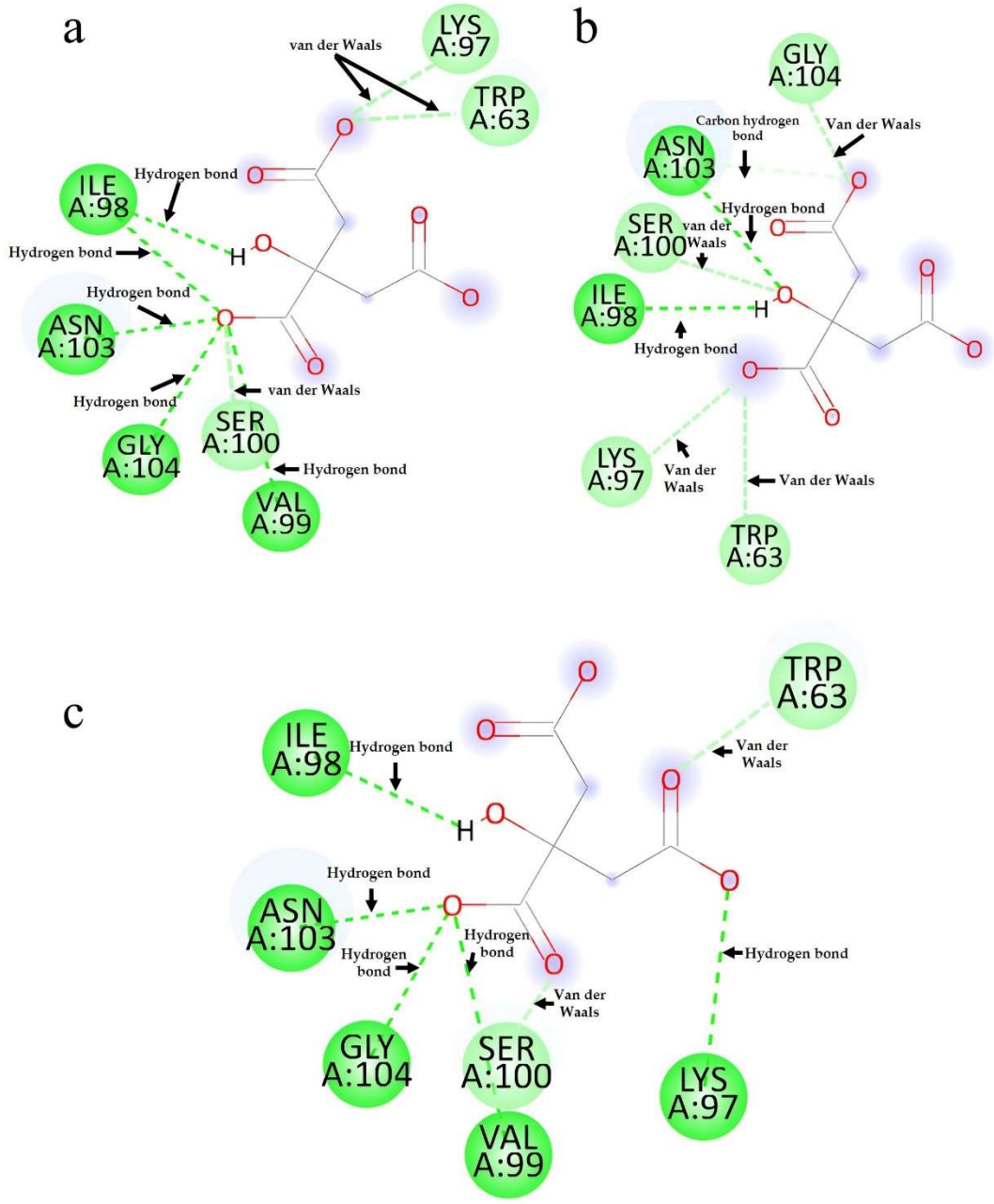

Figure 7. Citrate ion and Lyz coupling.

3.3.2. Adsorption isotherm

To determine the maximum adsorption capacity of coated nanoparticles, the adsorption isotherm was constructed. The graph of adsorption capacity (expressed in μg/mg) as a function of protein concentration (μg/mL) at equilibrium was fitted to the Langmuir [80] and Freundlich [81] adsorption models, respectively (see Figure 8). The statistical parameters R^2 (coefficient of determination) and RMSE (root mean square error) were used to evaluate the quality of the fits, confirming that the Langmuir adsorption model best fits the experimental data (see Table 3). In contrast to these results, there are studies demonstrating that protein adsorption on solid surfaces does not comply with the

assumptions of the Langmuir isotherm model [82,83], but rather, it is a much more complex process. Despite this, and due to the simplicity of its mathematical expression (Eq 3), the model is still used to estimate data such as the maximum adsorption capacity of an adsorbent.

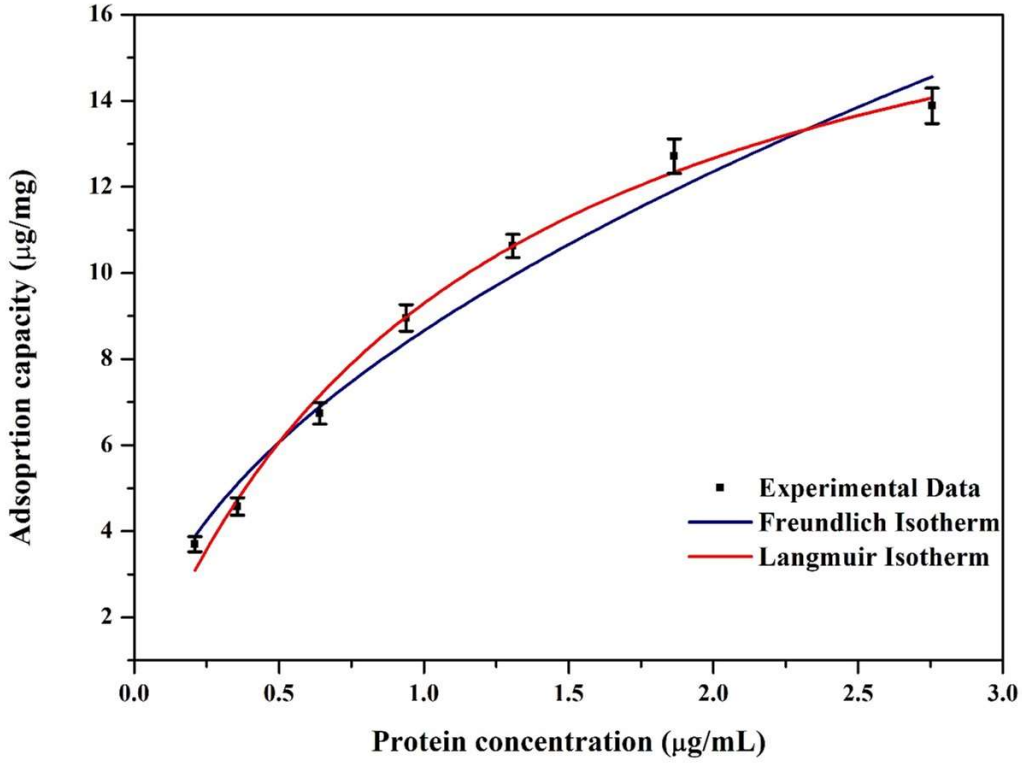

Figure 8. Fit of Lyz adsorption isotherm to Langmuir and Freundlich models.

Table 3. Estimated parameters of Langmuir and Freundlich models.

Isotherm model	Equation parameters			
	q_m (μg/mg)	K_L (mL/mg)	R^2	RSME
Langmuir model	19.9 ± 1.1*	0.88	0.99	0.35
Freundluich model	-	-	0.97	0.54

*Standard error.

$$q_e = \frac{q_m \times K_L \times C_{eq}}{1 + K_L \times C_{eq}} \tag{3}$$

where q_e and q_m (μg/mg) are the adsorption capacity of the adsorbent at equilibrium and the maximum adsorption capacity, respectively; K_L (mL/μg) is the Langmuir constant relative to the adsorption capacity; and C_{eq} is the concentration of the adsorbate once adsorption equilibrium is reached. The adsorption capacity was calculated using the Eq 4:

$$adsorption\ capacity\ \left(\frac{\mu g}{mg}\right) = \frac{C_0 - C_f}{m_{np}} \times V \tag{4}$$

where C_0 and C_f are the initial and final concentrations, respectively, of Lyz expressed in μg/mL; m_{np} is the amount, expressed in mg, of nanoparticles added to the vial; and V is the volume, in mL, of the protein solution placed in the vial [34].

In this case, a maximum adsorption capacity of 19.9 μg of protein per milligram of nanoparticles was achieved. Certainly, there are reports of nanoparticles, even without coating, used in protein adsorption, in which the amount of adsorbed protein was much higher than in our case [84–86]. However, the maximum initial protein concentration used for constructing our isotherm was 23.6 μg/mL; this value is considerably lower than those used in those reports (500 [84], 0.4 [85], 400 mg/mL [86]). Regarding this, there is evidence that the adsorption capacity shows a direct dependence on the initial protein concentration [37,87,88], which could explain the relatively low value of the adsorption capacity of IONPs@CA when compared to previous research. In addition to concentration, there are other experimental factors that significantly influence the adsorption process, such as pH, ionic strength of the medium, and temperature [89]. The optimization of these parameters in our experiments could result in an increase in the adsorption capacity of the nanoparticles.

However, besides the maximum adsorption capacity, the percentage of adsorbed protein (see Eq 1) can be used to evaluate the performance of the nanoparticles. For this calculation, the Lyz solution with the highest concentration (23.6 μg/mL) was used to estimate the maximum percentage of protein that could be adsorbed by IONPs@CA, which resulted in 88.3% ± 0.2%. Table 4 summarizes the performance of various molecules during the adsorption of lysozyme. As observed, citric acid has an efficiency of 88.3%, making it a very competitive adsorbent agent, outperforming succinic anhydride [90] and β-glucosidase [91].

Table 4. Adsorption efficiency using different coatings.

Coating agent	Adsorption efficiency	Reference
Succinic anhydride	62%	[90]
[1]LMW-polyacrylic acid	98%	[90]
[2]HMW-polyacrylic acid	100%	[90]
β-glucosidase	80%	[91]

1: Low molecular weight; 2: high molecular weight.

4. Conclusions

IONPs were successfully synthesized with a crystalline structure consistent with magnetite and maghemite phases of iron oxide using the coprecipitation method. These nanoparticles, with an average particle size of 8 nm, were further modified with citric acid, as confirmed by FT-IR spectroscopy and dynamic light scattering. The addition of new functional groups on the nanoparticle surface enhanced the colloidal stability of the material, indicated by the more negative Z potential values for the IONPs@AC compared to the uncoated nanoparticles. The hypothesis that the coating could improve the adsorption of Lyz onto nanoparticles was confirmed in in silico studies, achieving a maximum adsorption percentage of 88.3% after the surface modification of the nanoparticles. This underscores the effectiveness of surface modification in improving the adsorption capacity of the nanoparticles, which has significant implications for various biomedical and environmental applications.

Use of AI tools declaration

The authors declare they have not used Artificial Intelligence (AI) tools in the creation of this article.

Acknowledgments

The authors are grateful to the Instituto Politecnico Nacional for funding this research with SIP: 20230931 and 20230963 projects. Denise Arrozarena Portilla also acknowledges CONAHCYT for scholarship No. 931164. The authors acknowledge CNMN-IPN, Dr. Liliana Alamilla Beltrán and Dr. Gustavo. F. Gutiérrez-López (from ENCB), Dr. Claudia I. Hidalgo Moreno (from Colegio de Postgraduados) for the experimental support provided. The authors acknowledge Dr. Eduardo Gonzalez Martinez for his valuable suggestions.

Author contributions

Conceptualization: H. Y. M., R. M. E, D. A. P, A. A. V. L.; methodology: D. A. P and A. A. V. L; software: A. A. V. L.; validation: H. Y. M. and R. M. E.; formal analysis: D. A. P.; investigation: D. A. P.; resources: H. Y. M.; data curation: D. A. P. and A. A. V. L.; writing original draft preparation: D. A. P. and A. A. V. L; writing, review and editing: H. Y. M. and R. M. E.; supervision: R. M. E. and H. Y. M.; project administration: H. Y. M. and R. M. E.; funding acquisition: H. Y. M. and R. M. E. All authors have read and agreed to the published version of the manuscript.

Conflict of interest

The authors declare no conflict of interest.

References

1. Song YF, Feng LX, Basuray S, et al. (2023) Hemoglobin-BSA separation and purification by internally staged ultrafiltration. *Sep Purif Technol* 312: 123363. https://doi.org/10.1016/j.seppur.2023.123363
2. Ayan K, Ganar K, Deshpande S, et al. (2023) Continuous counter-current electrophoretic separation of oleosomes and proteins from oilseeds. *Food Hydrocolloid* 144: 109053. https://doi.org/10.1016/j.foodhyd.2023.109053
3. Gómez-García R, Campos DA, Aguilar C, et al. (2021) Biological protein precipitation: A green process for the extraction of cucumisin from melon (Cucumis melo L. inodorus) by-products. *Food Hydrocolloid* 116: 106650. https://doi.org/10.1016/j.foodhyd.2021.106650
4. Kanoh S, Shiraki K, Wada M, et al. (2023) Chromatographic purification of histidine-tagged proteins using zirconia particles modified with phosphate groups. *J Chromatogr A* 1703: 464112. https://doi.org/10.1016/j.chroma.2023.464112
5. Rodriguez EL, Poddar S, Iftekhar S, et al. (2020) Affinity chromatography: A review of trends and developments over the past 50 years. *J Chromatogr B* 1157: 122332. https://doi.org/10.1016/j.jchromb.2020.122332

6. Mahmoudi GM, Saraygord-Afshari N, Farsimadan M, et al. (2020) Opportunities and challenges of the tag-assisted protein purification techniques: Applications in the pharmaceutical industry. *Biotechnol Adv* 45: 107653. https://doi.org/10.1016/j.biotechadv.2020.107653
7. Chu W, Prodromou R, Day KN, et al. (2021) Peptides and pseudopeptide ligands: A powerful toolbox for the affinity purification of current and next-generation biotherapeutics. *J Chromatogr A* 1635: 461632. https://doi.org/10.1016/j.chroma.2020.461632
8. Huang H, Dong X, Sun Y, et al. (2023) Biomimetic affinity chromatography for antibody purification: Host cell protein binding and impurity removal. *J Chromatogr A* 1707: 464305. https://doi.org/10.1016/j.chroma.2023.464305
9. Hamedani NS, Happich FL, Klein EM, et al. (2022) Aptamer loaded superparamagnetic beads for selective capturing and gentle release of activated protein C. *Sci Rep* 12: 7091. https://doi.org/10.1038/s41598-022-11198-5
10. Perret G, Boschetti E (2020) Aptamer-based affinity chromatography for protein extraction and purification, In: Urmann K, Walter JG, *Advances in Biochemical Engineering/Biotechnology*, Cham: Springer. https://doi.org/10.1007/10_2019_106
11. Yıldırım D, Kip Ç, Tsogtbaatar K, et al. (2020) Microfluidic immobilized metal affinity chromatography based on Ti(IV)-decorated silica microspheres for purification of phosphoproteins. *J Chromatogr B* 1140: 122010. https://doi.org/10.1016/j.jchromb.2020.122010
12. Marini T, Gallina DA, Nabeshima EH, et al. (2022) Development of probiotic yoghurts with high protein content by ultrafiltration. *NFS J* 29: 16–25. https://doi.org/10.1016/j.nfs.2022.09.003
13. Çambay KF, Koçer İ, Kip Ç, et al. (2023) Ni(II) functionalized polyhedral oligomeric silsesquioxane based capillary monolith for purification of histidine-tagged proteins by immobilized metal affinity micro-chromatography. *J Chromatogr B* 1225: 123759. https://doi.org/10.1016/j.jchromb.2023.123759
14. Choi HJ, Cheong DE, Yoo SK, et al. (2023) One-step metal affinity purification of recombinant hFGF19 without using tags. *Protein Expr Purif* 201: 106186. https://doi.org/10.1016/j.pep.2022.106186
15. Hoffman DL (1989) Purification and large-scale preparation of antithrombin III. *Am J Med* 87: 23–26. https://doi.org/10.1016/0002-9343(89)80527-3
16. N'cho JS, Fofana I, Hadjadj Y, et al. (2016) Review of physicochemical-based diagnostic techniques for assessing insulation condition in aged transformers. *Energies* 9: 367. https://doi.org/10.3390/en9050367
17. Ali AH (2022) High-performance liquid chromatography (HPLC): A review. *Ann Adv Chem* 6: 010–020. https://doi.org/10.29328/journal.aac.1001026
18. Wang J, Han Q, Wang K, et al. (2023) Recent advances in development of functional magnetic adsorbents for selective separation of proteins/peptides. *Talanta* 253: 123919. https://doi.org/10.1016/j.talanta.2022.123919
19. Eivazzadeh-Keihan R, Bahreinizad H, Amiri Z, et al. (2021) Functionalized magnetic nanoparticles for the separation and purification of proteins and peptides. *TrAC Trends Anal Chem* 141: 116291. https://doi.org/10.1016/j.trac.2021.116291
20. Thomas SL, Thacker JB, Schug KA, et al. (2021) Sample preparation and fractionation techniques for intact proteins for mass spectrometric analysis. *J Sep Sci* 44: 211–246. https://doi.org/10.1002/jssc.202000936

21. Cai L, Gao Y, Chu Y, et al. (2023) Green synthesis of silica-coated magnetic nanocarriers for simultaneous purification-immobilization of β-1,3-xylanase. *Int J Biol Macromol* 233: 123223. https://doi.org/10.1016/j.ijbiomac.2023.123223
22. Wahajuddin, Arora S (2012) Superparamagnetic iron oxide nanoparticles: Magnetic nanoplatforms as drug carriers. *Int J Nanomedicine* 7: 3445–3471. https://doi.org/10.2147/IJN.S30320
23. Ghutepatil P, Khot VM, Salunkhe AB, et al. (2022) Design of monodispersed PVP functionalized biocompatible manganese ferrite nanoparticles for hyperthermia application. *Mater Today Proc* 62: 5341–5346. https://doi.org/10.1016/j.matpr.2022.03.417
24. Valdeperez D, Wutke N, Ackermann LM, et al. (2022) Colloidal stability of polymer coated zwitterionic Au nanoparticles in biological media. *Inorg Chim Acta* 534: 120820. https://doi.org/10.1016/j.ica.2022.120820
25. Amatya R, Lee D, Sultana M, et al. (2023) Albumin-coated copper nanoparticles for photothermal cancer therapy: Synthesis and in vitro characterization. *Heliyon* 9: 17732. https://doi.org/10.1016/j.heliyon.2023.e17732
26. Turrina C, Schoenen M, Milani D, et al. (2023) Application of magnetic iron oxide nanoparticles: Thrombotic activity, imaging and cytocompatibility of silica-coated and carboxymethyl dextran-coated particles. *Colloids Surf B Biointerfaces* 228: 113428. https://doi.org/10.1016/j.colsurfb.2023.113428
27. Zeng K, Sun EJ, Liu ZW, et al. (2020) Synthesis of magnetic nanoparticles with an IDA or TED modified surface for purification and immobilization of poly-histidine tagged proteins. *RSC Adv* 10: 11524–11534. https://doi.org/10.1039/C9RA10473A
28. Lodhi MS, Shaheen A, Khan MT, et al. (2022) A novel method of affinity purification and characterization of polygalacturonase of Aspergillus flavus by galacturonic acid engineered magnetic nanoparticle. *Food Chem* 372: 131317. https://doi.org/10.1016/j.foodchem.2021.131317
29. Tavakoli Z, Rasekh B, Yazdian F, et al. (2019) One-step separation of the recombinant protein by using the amine-functionalized magnetic mesoporous silica nanoparticles; an efficient and facile approach. *Int J Biol Macromol* 135: 600–608. https://doi.org/10.1016/j.ijbiomac.2019.05.114
30. Medina-Espinosa T, Asimbaya C, Galeas S, et al. (2021) Adsorptive removal of chromium (VI) from synthetic waters using magnetic lignocellulosic composites. *IOP Conf Ser Earth Environ Sci* 897: 012020. https://doi.org/10.1088/1755-1315/897/1/012020
31. Liu J, Dai C, Hu Y, et al. (2018) Aqueous aggregation behavior of citric acid coated magnetite nanoparticles: Effects of pH, cations, anions, and humic acid. *Environ Res* 161: 49–60. https://doi.org/10.1016/j.envres.2017.10.045
32. Bradford MM (1976) A rapid and sensitive method for the quantitation of microgram quantities of protein utilizing the principle of protein-dye binding. *Anal Biochem* 72: 248–254. https://doi.org/10.1016/0003-2697(76)90527-3
33. Rahman Z, Dong YL, Ren C, et al. (2012) Protein adsorption on citrate modified magnetic nanoparticles. *J Nanosci Nanotechnol* 12: 2598–2606. https://doi.org/10.1166/jnn.2012.5751
34. Yang X, Zhang H, Cheng S, et al. (2022) Optimization of the adsorption and removal of Sb(iii) by MIL-53(Fe)/GO using response surface methodology. *RSC Adv* 12: 4101–4112. https://doi.org/10.1039/d1ra08169a

35. Al-Madhagi H, Yazbik V, Abdelwahed W, et al. (2023) Magnetite nanoparticle co-precipitation synthesis, characterization, and applications: Mini review. *BioNanoScience* 13: 853–859. https://doi.org/10.1007/s12668-023-01113-1
36. Dubey M, Challagulla N, Wadhwa S, et al. (2021) Ultrasound assisted synthesis of magnetic Fe_3O_4/α-MnO_2 nanocomposite for photodegradation of organic dye. *Colloids Surf A* 609: 125720. https://doi.org/10.1016/j.colsurfa.2020.125720
37. González-Martínez DA, González G, Escalante-Bermúdez C, et al. (2023) Efficient capture of recombinant SARS-CoV-2 receptor-binding domain (RBD) with citrate-coated magnetic iron oxide nanoparticles. *Nanoscale* 15: 7854–7869. https://doi.org/10.1039/d3nr01109g
38. Kristianto H, Reynaldi E, Prasetyo S, et al. (2020) Adsorbed leucaena protein on citrate modified Fe_3O_4 nanoparticles: Synthesis, characterization, and its application as magnetic coagulant. *Sustain Environ Res* 30: 32. https://doi.org/10.1186/s42834-020-00074-4
39. Andronenko SI, Nikolaev AM, Suharzhevsky SM, et al. (2023) Phase composition and magnetic properties of nanoparticles with magnetite-maghemite structure. *Ceramics* 6: 1623–1631. https://doi.org/10.3390/ceramics6030099
40. Petcharoen K, Sirivat A (2012) Synthesis and characterization of magnetite nanoparticles via the chemical co-precipitation method. *Mater Sci Eng B* 177: 421–427. https://doi.org/10.1016/j.mseb.2012.01.003
41. González-Martínez E, Gómez A, González-Martínez DA, et al. (2021) Chitosan-coated magnetic nanoparticles; exploring their potentialities for DNA and Cu(II) recovery. *Inorg Nano-Met Chem* 51: 1098–1107. https://doi.org/10.1080/24701556.2020.1814335
42. Augusto-Jimenez YE, González-Montoya M, Naranjo-Feliciano D, et al. (2021) Antioxidant activity of bioactive peptide fractions from germinated soybeans conjugated to Fe_3O_4 nanoparticles by the Ugi multicomponent reaction. *Molecules* 26: 5726. https://doi.org/10.3390/molecules26195726
43. Peternele WS, Monge-Fuentes V, Fascineli ML, et al. (2014) Experimental investigation of the coprecipitation method: An approach to obtain magnetite and maghemite nanoparticles with improved properties. *J Nanomater* 2014: 682985. https://doi.org/10.1155/2014/682985
44. Kim W, Suh CY, Cho SW, et al. (2012) A new method for the identification and quantification of magnetite-maghemite mixture using conventional X-ray diffraction technique. *Talanta* 94: 348–352. https://doi.org/10.1016/j.talanta.2012.03.001
45. Freire TM, Dutra LMU, Queiroz DC, et al. (2016) Fast ultrasound assisted synthesis of chitosan-based magnetite nanocomposites as a modified electrode sensor. *Carbohydr Polym* 151: 760–769. https://doi.org/10.1016/j.carbpol.2016.05.095
46. Velásquez AA, Urquijo JP (2021) Synthesis and characterization of magnetite-maghemite nanoparticles in presence of polyethylene glycol obtained by mechanical milling. *Mater Sci Eng B* 263: 114873. https://doi.org/10.1016/j.mseb.2020.114873
47. Qureashi A, Pandith AH, Bashir A, et al. (2021) Citrate coated magnetite: A complete magneto dielectric, electrochemical and DFT study for detection and removal of heavy metal ions. *Surf Interfaces* 23: 101004. https://doi.org/10.1016/j.surfin.2021.101004
48. Shabatina TI, Vernaya OI, Shabatin VP, et al. (2020) Magnetic nanoparticles for biomedical purposes: Modern trends and prospects. *Magnetochemistry* 6: 30. https://doi.org/10.3390/magnetochemistry6030030

49. Dolai J, Mandal K, Jana NR, et al. (2021) Nanoparticle size effects in biomedical applications. *ACS Appl Nano Mater* 4: 6471–6496. https://doi.org/10.1021/acsanm.1c00987
50. Li L, Mak KY, Leung CW, et al. (2013) Effect of synthesis conditions on the properties of citric-acid coated iron oxide nanoparticles. *Microelectron Eng* 110: 329–334. https://doi.org/10.1016/j.mee.2013.02.045
51. Atrei A, Mahdizadeh FF, Baratto MC, et al. (2021) Effect of citrate on the size and the magnetic properties of primary Fe_3O_4 nanoparticles and their aggregates. *Appl Sci* 11: 6974. https://doi.org/10.3390/app11156974
52. Chesnel K, Trevino M, Cai Y, et al. (2014) Particle size effects on the magnetic behaviour of 5 to 11 nm Fe_3O_4 nanoparticles coated with oleic acid. *J Phys Conf Ser* 521: 012004. https://doi.org/10.1088/1742-6596/521/1/012004
53. Maleki H, Simchi A, Imani M, et al. (2012) Size-controlled synthesis of superparamagnetic iron oxide nanoparticles and their surface coating by gold for biomedical applications. *J Magn Magn Mater* 324: 3997–4005. https://doi.org/10.1016/j.jmmm.2012.06.045
54. Surpi A, Shelyakova T, Murgia M, et al. (2023) Versatile magnetic configuration for the control and manipulation of superparamagnetic nanoparticles. *Sci Rep* 13: 5301. https://doi.org/10.1038/s41598-023-32299-9
55. Hah HY, Gray S, Johnson CE, et al. (2021) Mössbauer spectroscopy of superparamagnetic Fe_3O_4 nanoparticles. *J Magn Magn Mater* 539: 168382. https://doi.org/10.1016/j.jmmm.2021.168382
56. Araujo JF, Tahir, Arsalani S, et al. (2020) Novel scanning magnetic microscopy method for the characterization of magnetic nanoparticles. *J Magn Magn Mater* 499: 166300. https://doi.org/10.1016/j.jmmm.2019.166300
57. Rezanezhad A, Hajalilou A, Eslami F, et al. (2021) Superparamagnetic magnetite nanoparticles for cancer cells treatment via magnetic hyperthermia: Effect of natural capping agent, particle size and concentration. *J Mater Sci Mater Electron* 32: 24026–24040. https://doi.org/10.1007/s10854-021-06865-8
58. Abdolrahimi M, Vasilakaki M, Slimani S, et al. (2021) Magnetism of nanoparticles: Effect of the organic coating. *Nanomaterials* 11: 1787. https://doi.org/10.3390/nano11071787
59. Guduri BR, Luyt AS (2008) Structure and mechanical properties of polycarbonate modified clay nanocomposites. *J Nanosci Nanotechnol* 8: 1880–1885. https://doi.org/10.1166/jnn.2008.18253
60. Omelyanchik A, Gomes da Silva F, Gomide G, et al. (2021) Effect of citric acid on the morpho-structural and magnetic properties of ultrasmall iron oxide nanoparticles. *J Alloys Compd* 883: 160779. https://doi.org/10.1016/j.jallcom.2021.160779
61. Blanco-Andujar C, Ortega D, Southern P, et al. (2015) High performance multi-core iron oxide nanoparticles for magnetic hyperthermia: Microwave synthesis, and the role of core-to-core interactions. *Nanoscale* 7: 1768–1775. https://doi.org/10.1039/c4nr06239f
62. Walkey CD, Olsen JB, Guo H, et al. (2012) Nanoparticle size and surface chemistry determine serum protein adsorption and macrophage uptake. *J Am Chem Soc* 134: 2139–2147. https://doi.org/10.1021/ja2084338
63. Ibrahim MA, Jaafar MZ, Yusof MA, et al. (2023) Influence of size and surface charge on the adsorption behaviour of silicon dioxide nanoparticles on sand particles. *Colloids Surf A* 674: 131943. https://doi.org/10.1016/j.colsurfa.2023.131943

64. Dongargaonkar AA, Clogston JD (2018) Quantitation of surface coating on nanoparticles using thermogravimetric analysis. *Methods Mol Biol* 1682: 57–63. https://doi.org/10.1007/978-1-4939-7352-1_6
65. Malik LA, Bashir A, Ahmad N, et al. (2020) Exploring metal ion adsorption and antifungal properties of carbon-coated magnetite composite. *ChemistrySelect* 5: 3208–3216. https://doi.org/10.1002/slct.201904830
66. Hancock ML, Yokel RA, Beck MJ, et al. (2021) The characterization of purified citrate-coated cerium oxide nanoparticles prepared via hydrothermal synthesis. *Appl Surf Sci* 535: 147681. https://doi.org/10.1016/j.apsusc.2020.147681
67. Vassallo M, Martella D, Barrera G, et al. (2023) Improvement of hyperthermia properties of iron oxide nanoparticles by surface coating. *ACS Omega* 8: 2143–2154. https://doi.org/10.1021/acsomega.2c06244
68. Jia ZX, Li JT, Gao L, et al. (2023) Dynamic light scattering: A powerful tool for in situ nanoparticle sizing. *Colloids Interfaces* 7: 15. https://doi.org/10.3390/colloids7010015
69. Jummes B, Sganzerla WG, Gonçalves da Rosa G, et al. (2020) Antioxidant and antimicrobial poly-ε-caprolactone nanoparticles loaded with Cymbopogon martinii essential oil. *Biocatal Agric Biotechnol* 23: 101499. https://doi.org/10.1016/j.bcab.2020.101499
70. Joseph E, Singhvi G (2019) Chapter 4—Multifunctional nanocrystals for cancer therapy: A potential nanocarrier, In: Grumezescu AM, *Nanomaterials for Drug Delivery and Therapy*, Norwich: William Andrew Publishing, 91–116. https://doi.org/10.1016/b978-0-12-816505-8.00007-2
71. Dheyab MA, Aziz AA, Jameel MS, et al. (2020) Simple rapid stabilization method through citric acid modification for magnetite nanoparticles. *Sci Rep* 10: 10793. https://doi.org/10.1038/s41598-020-67869-8
72. Stein R, Friedrich B, Mühlberger M, et al. (2020) Synthesis and characterization of citrate-stabilized gold-coated superparamagnetic iron oxide nanoparticles for biomedical applications. *Molecules* 25: 4425. https://doi.org/10.3390/molecules25194425
73. Raji Z, Karim A, Karam A, et al. (2023) A review on the heavy metal adsorption capacity of dietary fibers derived from agro-based wastes: Opportunities and challenges for practical applications in the food industry. *Trends Food Sci Technol* 137: 74–91. https://doi.org/10.1016/j.tifs.2023.05.004
74. Alderton G, Fevold HL (1946) Direct crystallization of lysozyme from egg white and some crystalline salts of lysozyme. *J Biol Chem* 164: 1–5. https://doi.org/10.1016/S0021-9258(18)43040-2
75. Abdelsattar AS, Dawoud A, Helal MA (2021) Interaction of nanoparticles with biological macromolecules: A review of molecular docking studies. *Nanotoxicology* 15: 66–95. https://doi.org/10.1080/17435390.2020.1842537
76. Maulydia NB, Tallei TE, Ginting B, et al. (2022) Analysis of flavonoid compounds of Orange (Citrus sp.) peel as anti-main protease of SARS-CoV-2: A molecular docking study. *IOP Conf Ser Earth Environ Sci* 951: 012078. https://doi.org/10.1088/1755-1315/951/1/012078
77. Weinhold F, Klein RA (2014) Anti-electrostatic hydrogen bonds. *Angew Chem Int Ed* 53: 11214–11217. https://doi.org/10.1002/anie.201405812

78. Vaidyanathan R, Murugan SS, Ravichandran K, et al. (2023) Molecular docking approach on the binding stability of derivatives of phenolic acids (DPAs) with human serum albumin (HSA): Hydrogen-bonding versus hydrophobic interactions or combined influences? *JCIS Open* 12: 100096. https://doi.org/10.1016/j.jciso.2023.100096
79. Pinzi L, Rastelli G (2019) Molecular docking: Shifting paradigms in drug discovery. *Int J Mol Sci* 20: 4331. https://doi.org/10.3390/ijms20184331
80. Langmuir I (1916) The constitution and fundamental properties of solids and liquids. Part I. Solids. *J Am Chem Soc* 38: 2221–2295. https://doi.org/10.1021/ja02268a002
81. Singh AK (2016) Chapter 8—Nanoparticle ecotoxicology, In: Singh AK, *Engineered Nanoparticles*, Boston: Academic Press, 343–350. http://dx.doi.org/10.1016/b978-0-12-801406-6.00008-x
82. Cho M, Mahmoodi Z, Shetty P, et al. (2024) Protein adsorption on solid surfaces: Data mining, database, molecular surface-derived properties, and semiempirical relationships. *ACS Appl Mater Interfaces* 16: 28290–28306. https://doi.org/10.1021/acsami.4c06759
83. Latour RA (2015) The Langmuir isotherm: A commonly applied but misleading approach for the analysis of protein adsorption behavior. *J Biomed Mater Res A* 103: 949–958. https://doi.org/10.1002/jbm.a.35235
84. Rahdar S, Rahdar A, Ahmadi S, et al. (2019) Adsorption of bovine serum albumin (BSA) by bare magnetite nanoparticles with surface oxidative impurities that prevent aggregation. *Can J Chem* 97: 577–583. https://doi.org/10.1139/cjc-2019-0008
85. Zhang J, Huang L, Zheng J, et al. (2020) SiO_2-assisted synthesis of Fe_3O_4@SiO_2@C-Ni nanochains for effective catalysis and protein adsorption. *J Magn Magn Mater* 497: 166011. https://doi.org/10.1016/j.jmmm.2019.166011
86. Maleki MS, Moradi O, Tahmasebi S (2017) Adsorption of albumin by gold nanoparticles: Equilibrium and thermodynamics studies. *Arab J Chem* 7: 1104–1109. https://doi.org/10.1016/j.arabjc.2012.09.003
87. Wang G, Hou H, Wang S, et al. (2017) Exploring the interaction of silver nanoparticles with lysozyme: Binding behaviors and kinetics. *Colloids Surf B Biointerfaces* 1: 138–145. https://doi.org/10.1016/j.colsurfb.2017.05.071
88. Saptarshi SR, Duschl A, Lopata AL (2013) Interaction of nanoparticles with proteins: Relation to bio-reactivity of the nanoparticle. *J Nanobiotechnol* 11: 26. https://doi.org/10.1186/1477-3155-11-26
89. Rabe M, Verdes D, Seeger S (2011) Understanding protein adsorption phenomena at solid surfaces. *Adv Colloid Interface Sci* 162: 87–106. https://doi.org/10.1016/j.cis.2010.12.007
90. Esmaeilnejad-Ahranjani P, Maboudi SA, Arpanaei A (2023) Effect of the structure of magnetic nanocomposite adsorbents on the lysozyme separation efficiency. *ACS Appl Bio Mater* 6: 191–202. https://doi.org/10.1016/j.mtcomm.2023.105632
91. Pota G, Gallucci N, Cavasso D, et al. (2023) Controlling the adsorption of β-glucosidase onto wrinkled SiO_2 nanoparticles to boost the yield of immobilization of an efficient biocatalyst. *Langmuir* 39: 1482–1494. https://doi.org/10.1021/acs.langmuir.2c02861

AIMS Press